Modelling and Removing Radial and Tangential Distortions in Spherical Lenses

S.S. Beauchemin and R. Bajcsy

[1] Dept. of Computer Science
University of Western Ontario
London, Ontario, Canada, N6A 5B7
beau@csd.uwo.ca
[2] GRASP Laboratory
University of Pennsylvania
Philadelphia PA 19104-6228 USA
bajcsy@central.cis.upenn.edu

Abstract

Spherical cameras are variable-resolution imaging systems and promising devices for autonomous navigation purposes, mainly because of their wide viewing angle which increases the capabilities of vision-based obstacle avoidance schemes. In addition, spherical lenses resemble the primate eye in their projective models and are biologically relevant. However, the calibration of spherical lenses for Computer Vision is a recent research topic and current procedures for pinhole camera calibration are inadequate when applied to spherical lenses. We present a novel method for spherical-lens camera calibration which models the lens radial and tangential distortions and determines the optical center and the angular deviations of the CCD sensor array within a unified numerical procedure. Contrary to other methods, there is no need for special equipment such as low-power laser beams or non-standard numerical procedures for finding the optical center. Numerical experiments, convergence and robustness analyses are presented.

1 Introduction

Spherical cameras are variable-resolution imaging systems useful for autonomous navigation purposes, mainly because of their wide viewing angle which increases the capabilities of vision-based obstacle avoidance schemes [11]. In addition, spherical lenses resemble the primate eye in their projective models and are biologically relevant [4]. In spite of this, the calibration of spherical lenses is not well understood [10] and contributions to this topic have only recently begun to appear in the literature.

Current standard procedures for pinhole camera calibration are inadequate for spherical lenses as such devices introduce significant amounts of image distortion. Calibration methods such as Tsai's [13] only consider the first term of radial distortion which is insufficient to account for the distortion typically induced by spherical lenses. Other calibration procedures for high distortion and spherical lenses such as Shah and Aggarwal's [9] and Basu and Licradie's [3] have been defined. However, these methods use special equipment such as low-power

laser beams or ad-hoc numerical procedures for determining the optical center of spherical lenses. We propose a novel method which only requires an adequate calibration plane and a unified numerical procedure for determining the optical center, among other intrinsic parameters.

1.1 Types of Distortion

The calibration of optical sensors in computer vision is an important issue in autonomous navigation, stereo vision and numerous other applications where accurate positional observations are required. Various techniques have been developed for the calibration of sensors based on the traditional pinhole camera model. Typically, the following types of geometrical distortion have been recognized and dealt with [14]:

- **Radial Distortion:** This type of distortion is point-symmetric at the optical center of the lens and causes an inward or outward shift of image points from their initial perspective projection. About the optical center, radial distortion is expressed as

$$\hat{r} = r + \kappa_1 r^3 + \kappa_2 r^5 + \kappa_3 r^7 + \cdots, \tag{1}$$

  where κ_i are radial distortion coefficients, r is the observed radial component of a projected point and $\hat{r}$, its predicted perspective projection [7].
- **Decentering Distortion:** The misalignment of the optical centers of various lens elements in the sensor induces a decentering distortion which has both a radial and a tangential component. They are expressed as

$$\begin{aligned} \hat{r} &= r + 3(\eta_1 r^2 + \eta_2 r^4 + \eta_3 r^6 + \cdots)\sin(\theta - \theta_0) \\ \hat{\theta} &= \theta + (\eta_1 r^2 + \eta_2 r^4 + \eta_3 r^6 + \cdots)\cos(\theta - \theta_0), \end{aligned} \tag{2}$$

  where η_i are the decentering distortion coefficients, θ is the observed angular component of a projected point, $\hat{\theta}$ is its predicted perspective projection and θ_0 is the angle between the positive y-axis and the axis of maximum tangential distortion due to decentering [7].
- **Thin Prism:** Manufacturing imperfections of lens elements and misalignment of CCD sensor arrays from thier ideal, perpendicular orientation to the optical axis introduce additional radial and tangential distortions which are given by

$$\begin{aligned} \hat{r} &= r + (\zeta_1 r^2 + \zeta_2 r^4 + \zeta_3 r^6 + \cdots)\sin(\theta - \theta_1) \\ \hat{\theta} &= \theta + (\zeta_1 r^2 + \zeta_2 r^4 + \zeta_3 r^6 + \cdots)\cos(\theta - \theta_1), \end{aligned} \tag{3}$$

  where ζ_i are the thin prism distortion coefficients and θ_1 is the angle between the positive y-axis and the axis of maximum tangential distortion due to thin prism [7].

1.2 Related Literature

The need for foveated visual fields in active vision applications has motivated the design of special-purpose spherical lenses [4] and catadioptric sensors [2]. These imaging systems introduce significant amounts of radial and possibly tangential distortions (see Figure 2) and traditional methods that only calibrate for the perspective projection matrix and neglect to compensate for these distortions are inadequate [12].

The calibration methods designed for high-distortion lenses typically model the radial and tangential distortion components with polynomial curve-fitting. Examples of such methods are Shah and Aggarwal's [10] and Basu and Licardie's [3]. Both of these methods calibrate the optical center by using procedures that are not elegantly integrated into the curve-fitting procedure which recovers distortion coefficients. For instance, Basu and Licaride's method consists of a minimization of vertical and horizontal calibration-line curvatures whereas Shah and Aggarwal's requires the use of a low-power laser beam based on a partial reflection beam-alignment technique.

Other, similar methods perform minimizations of functionals representing measures of the accuracy of the image transformation with respect to calibration parameters [6, 14]. These methods rely on the point-symmetry of radial distortion at the location of the optical center onto the image plane to reduce the dimensionality of the parameter space [6] or to iteratively refine calibration parameters initially obtained with a distortion-free pinhole camera model [14].

In addition to these calibration techniques, Miyamoto [5] defined mappings relating the world plane angle θ_1 to the image plane angle θ_2. One such mapping is given by $\theta_2 = \tan\theta_1$ (see Figure 1). Alternatively, Anderson *et al.* [1] defined a similar mapping this time based on Snell's law of diffraction. Unfortunately, the accuracy of these models is limited to the neighborood of the optical center [10]. Basu and Licardie also proposed alternative models for fish-eye lenses based in log-polar transformations [3] but, in this case, they demonstrate that the small number of calibration parameters does not permit to accurately model a spherical lens.

2 Standard Procedure for Fish-Eye Lens Calibration

The number of free intrinsic parameters for a typical high distortion lens is large, especially when one considers sources or radial distortions, decentering and thin prism, manufacturing misalignments such as tilt, yaw and roll angles of the CCD sensor array with respect to its ideal position, image center versus optical center, *etc.* We encompass radial and tangential distortions in two polynomials for which the coefficients are to be determined with respect to the sources of distortion emanating from the location of the optical center and the pitch and yaw angles of the CCD sensor. We proceed by describing the least-squares method chosen to perform the polynomial fits for both radial and tangential distortions.

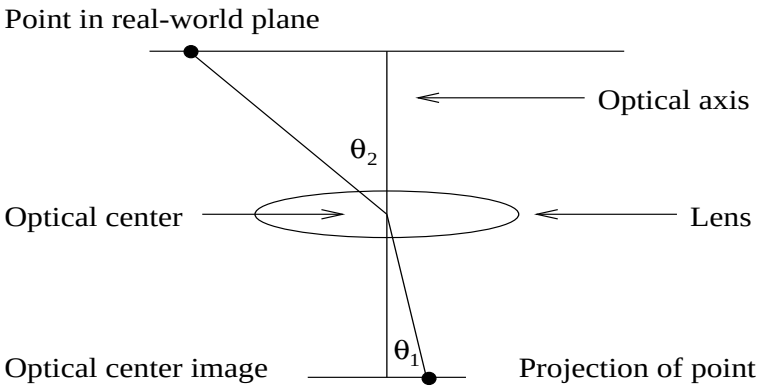

Fig. 1. *The image plane and world plane angles θ_1 and θ_2 are the angles formed by the projective rays between the image plane and the world plane, both orthogonal to the optical axis.*

2.1 Radial and Tangential Polynomials

Given a set of calibration points and their image locations, the equations describing the transformation from fish-eye to pinhole are

$$\hat{\theta}_{ij} = \sum_{k=0}^{L} a_k \theta_{ij}^k \quad \text{and} \quad \hat{r}_{ij} = \sum_{k=0}^{L} b_k r_{ij}^k \tag{4}$$

where L is the order of the polynomials and $\hat{\theta}_{ij}$ and $\hat{r}_{ij}$ are the corrected polar coordinates of the calibration points. We use a calibration pattern for which the points align into horizontal, diagonal and vertical lines. These n^2 calibration points may be arranged in matrix form consistent with their geometric location on the calibration plane:

$$\begin{bmatrix} \mathbf{P}_{11} & \mathbf{P}_{12} & \cdots & \mathbf{P}_{1n} \\ \mathbf{P}_{21} & \mathbf{P}_{22} & \cdots & \mathbf{P}_{2n} \\ \vdots & & & \\ \mathbf{P}_{n1} & \mathbf{P}_{n2} & \cdots & \mathbf{P}_{nn} \end{bmatrix} \begin{bmatrix} \hat{\mathbf{p}}_{11} & \hat{\mathbf{p}}_{12} & \cdots & \hat{\mathbf{p}}_{1n} \\ \hat{\mathbf{p}}_{21} & \hat{\mathbf{p}}_{22} & \cdots & \hat{\mathbf{p}}_{2n} \\ \vdots & & & \\ \hat{\mathbf{p}}_{n1} & \hat{\mathbf{p}}_{n2} & \cdots & \hat{\mathbf{p}}_{nn} \end{bmatrix} \begin{bmatrix} \mathbf{p}_{11} & \mathbf{p}_{12} & \cdots & \mathbf{p}_{1n} \\ \mathbf{p}_{21} & \mathbf{p}_{22} & \cdots & \mathbf{p}_{2n} \\ \vdots & & & \\ \mathbf{p}_{n1} & \mathbf{p}_{n2} & \cdots & \mathbf{p}_{nn} \end{bmatrix} \tag{5}$$

where $\mathbf{P}_{ij} = (X_{ij}, Y_{ij}, Z_{ij})$ are the 3D calibration points expressed in the coordinate system of the camera, $\hat{\mathbf{p}}_{ij} = (\hat{r}_{ij}, \hat{\theta}_{ij})$ are the 2D projection of $\mathbf{P}_{ij}$ onto the pinhole camera and $\mathbf{p}_{ij} = (r_{ij}, \theta_{ij})$ are projection of $\mathbf{P}_{ij}$ as imaged by the spherical lens.

Various minimization methods may be applied to the polynomials in order to determine their coefficients. For instance, Lagrangian minimzation and least-squares have been used. For our purposes, we adopt a least-squares approach to

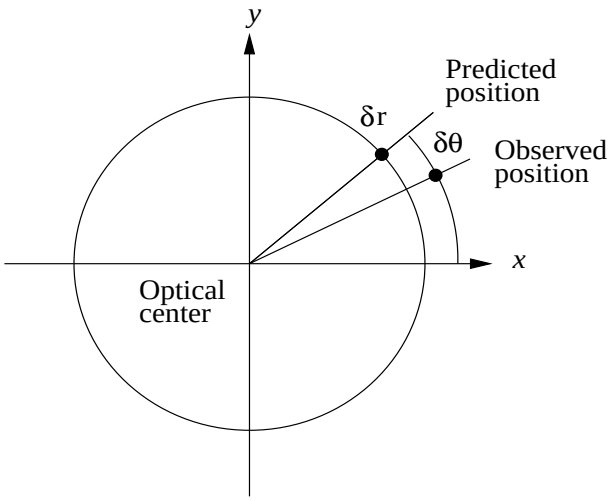

Fig. 2. *Radial and tangential distortions. The original point, expressed as* (r, θ) *is the expected observation. The distorted point as observed, is expressed as* $(r + \delta r, \theta + \delta\theta)$*, where* δr *and* $\delta\theta$ *are the radial and tangential distortions, respectively.*

find the polynomial coefficients and perform the correction. This least-squares fit for the radial and tangential distortion polynomial can be expressed as

$$\sum_{i=1}^{n}\sum_{j=1}^{n}\left(\hat{\theta}_{ij} - \sum_{k=0}^{L} a_k \theta_{ij}^k\right)^2 \quad \text{and} \quad \sum_{i=1}^{n}\sum_{j=1}^{n}\left(\hat{r}_{ij} - \sum_{k=0}^{L} b_k r_{ij}^k\right)^2. \tag{6}$$

Deriving the polynomials with respect to coefficients yields the following systems of linear equations

$$\mathbf{a}^T \boldsymbol{\Theta} = \theta_{ij}\boldsymbol{\theta}_{ij} \quad \text{and} \quad \mathbf{b}^T \mathbf{R}_{ij} = \hat{r}_{ij}\mathbf{r}_{ij} \tag{7}$$

where

$$\begin{aligned}
\mathbf{a} &= (a_0, \ldots, a_L)^T \\
\mathbf{b} &= (b_0, \ldots, b_L)^T \\
\mathbf{r}_{ij} &= (r_{ij}^0, \ldots, r_{ij}^L)^T \\
\boldsymbol{\theta}_{ij} &= (\theta_{ij}^0, \ldots, \theta_{ij}^L)^T \\
\mathbf{R}_{ij} &= \mathbf{r}_{ij}\mathbf{r}_{ij}^T \\
\boldsymbol{\Theta}_{ij} &= \boldsymbol{\theta}_{ij}\boldsymbol{\theta}_{ij}^T.
\end{aligned}$$

We write the general least-squares system of equations in matrix form as

$$\begin{aligned}
\sum_{i=1}^{n}\sum_{j=1}^{n}\sum_{k=0}^{L} b_k r_{ij}^k r_{ij}^0 &= \sum_{i=1}^{n}\sum_{j=1}^{n} \hat{r}_{ij} r_{ij}^0 \\
\sum_{i=1}^{n}\sum_{j=1}^{n}\sum_{k=0}^{L} b_k r_{ij}^k r_{ij}^1 &= \sum_{i=1}^{n}\sum_{j=1}^{n} \hat{r}_{ij} r_{ij}^1 \\
&\vdots \quad \vdots \\
\sum_{i=1}^{n}\sum_{j=1}^{n}\sum_{k=0}^{L} b_k r_{ij}^k r_{ij}^L &= \sum_{i=1}^{n}\sum_{j=1}^{n} \hat{r}_{ij} r_{ij}^L
\end{aligned} \tag{8}$$

and

$$\begin{aligned}
\sum_{i=1}^{n}\sum_{j=1}^{n}\sum_{k=0}^{L} a_k \theta_{ij}^k \theta_{ij}^0 &= \sum_{i=1}^{n}\sum_{j=1}^{n} \hat{\theta}_{ij} \theta_{ij}^0 \\
\sum_{i=1}^{n}\sum_{j=1}^{n}\sum_{k=0}^{L} b_k \theta_{ij}^k \theta_{ij}^1 &= \sum_{i=1}^{n}\sum_{j=1}^{n} \hat{\theta}_{ij} \theta_{ij}^1 \\
&\vdots \quad \vdots \\
\sum_{i=1}^{n}\sum_{j=1}^{n}\sum_{k=0}^{L} b_k r_{ij}^k \theta_{ij}^L &= \sum_{i=1}^{n}\sum_{j=1}^{n} \hat{\theta}_{ij} \theta_{ij}^L
\end{aligned} \tag{9}$$

The least-squares matrices may be written as

$$\mathbf{A}_r = \begin{pmatrix} r_{11}^0 & \cdots & r_{11}^L \\ r_{12}^0 & \cdots & r_{12}^L \\ \vdots & \vdots & \vdots \\ r_{1n}^0 & \cdots & r_{1n}^L \\ r_{21}^0 & \cdots & r_{2n}^L \\ \vdots & \vdots & \vdots \\ r_{nn}^0 & \cdots & r_{nn}^L \end{pmatrix} \quad \mathbf{A}_\theta = \begin{pmatrix} \theta_{11}^0 & \cdots & \theta_{11}^L \\ \theta_{12}^0 & \cdots & \theta_{12}^L \\ \vdots & \vdots & \vdots \\ \theta_{1n}^0 & \cdots & \theta_{1n}^L \\ \theta_{21}^0 & \cdots & \theta_{2n}^L \\ \vdots & \vdots & \vdots \\ \theta_{nn}^0 & \cdots & \theta_{nn}^L \end{pmatrix} \tag{10}$$

and we form the least-squares systems of equations as $\mathbf{R}_\theta \mathbf{a} = \boldsymbol{\theta}$ and $\mathbf{R}_r \mathbf{b} = \mathbf{r}$, where $\mathbf{R}_\theta = \mathbf{A}_\theta^T \mathbf{A}_\theta$, $\mathbf{R}_r = \mathbf{A}_r^T \mathbf{A}_r$, $\mathbf{r} = \mathbf{A}_r^T \mathbf{c}_r$, $\boldsymbol{\theta} = \mathbf{A}_\theta^T \mathbf{c}_\theta$ and

$$\mathbf{c}_\theta = \begin{pmatrix} \hat{\theta}_{11} \\ \hat{\theta}_{12} \\ \vdots \\ \hat{\theta}_{nn} \end{pmatrix} \quad \mathbf{c}_r = \begin{pmatrix} \hat{r}_{11} \\ \hat{r}_{12} \\ \vdots \\ \hat{r}_{nn} \end{pmatrix}$$

The coefficients $\mathbf{a}$ and $\mathbf{b}$ are such that they should minimze $\chi_\theta^2 = |\mathbf{A}_\theta \mathbf{a} - \mathbf{c}_\theta|^2$ and $\chi_r^2 = |\mathbf{A}_r \mathbf{b} - \mathbf{c}_r|^2$. We use Singular Value Decomposition (SVD) to perform

the least-squares fits

$$\mathbf{a} = \mathbf{V}_\theta \, \mathrm{diag}(\mathbf{W}_\theta)(\mathbf{U}_\theta^T \mathbf{c}_\theta) \tag{11}$$

$$\mathbf{b} = \mathbf{V}_\mathbf{r} \mathrm{diag}(\mathbf{W}_r)(\mathbf{U}_r^T \mathbf{c}_r) \tag{12}$$

where $\mathbf{A}_\theta = \mathbf{U}_\theta \mathbf{W}_\theta \mathbf{V}_\theta^T$ and $\mathbf{A}_r = \mathbf{U}_r \mathbf{W}_r \mathbf{V}_r^T$, and to compute χ_θ^2 and χ_r^2. We use the notation $\mathbf{a}(\mathbf{x}_c, \mathbf{x}_p)$, $\mathbf{b}(\mathbf{x}_c, \mathbf{x}_p, \theta_\mathbf{u}, \theta_\mathbf{v})$, $\chi_\theta^2(\mathbf{x}_c, \mathbf{x}_p)$ and $\chi_r^2(\mathbf{x}_c, \mathbf{x}_p, \theta_\mathbf{u}, \theta_\mathbf{v})$ to indicate that the least-squares solutions for tangential distortion coefficients $\mathbf{a}$ and the residual χ_θ^2 depend on $\mathbf{x}_c$, the location of the optical center with respect to the coordinate system in which the fit is performed and $\mathbf{x}_p$, the translation parallel to the calibration surface, and that the radial distortion coefficients $\mathbf{b}$ and the residual χ_r^2 depend on the optical center $\mathbf{x}_c$, the camera translation $\mathbf{x}_p$ and $\theta_\mathbf{u}$ and $\theta_\mathbf{v}$, the pitch and yaw angles of the CCD sensor array with respect to a plane perpendicular to the optical axis. We further explain and experimentally demonstrate these dependencies in sections 2.3 and 2.4.

2.2 Polynomial Order

The overfit of data, or polynomial orders that exceed the intrinsic order of the data, constitutes our primary motivation for using SVD in the least-squares solutions of the polynomial coefficients. For instance, if any of the singular values is less than a tolerance level of 10^{-5}, we set its reciprocal to zero, rather than letting it go to some arbitrarily high value. We thus avoid overfits of the calibration data when solving for $\mathbf{a}(\mathbf{x}_c, \mathbf{x}_p)$ and $\mathbf{b}(\mathbf{x}_c, \mathbf{x}_p, \theta_\mathbf{u}, \theta_\mathbf{v})$ in (11) and (12). Because of this capability and considering that the computational cost of calibration is usually not critical when compared with real-time vision computations, we use polynomials of order $L = 12$.

2.3 The Optical Center

The optical center of a lens is defined as the point where the optical axis passing through the lens intersects the image plane of the camera. Alternatively, the optical center is the image point where no distortions appear, radial or tangential. That is to say, where $\hat{r}_{ij} = r_{ij}$ and $\hat{\theta}_{ij} = \theta_{ij}$. In addition, radial distortion is point-symmetric at the optical center and, consequently, the one-dimensional polynomial in r is accurate only when aligned with the optical center. Figure 3 shows plots of $(\hat{r}_{ij}, r_{ij})$ and $(\hat{\theta}_{ij}, \theta_{ij})$ at and away from the optical center, in which the point-scattering effect becomes apparent as the ploynomial fit is gradually decentered from the optical center. This effect is reflected in the values of $\chi_r^2(\mathbf{x}_c, \mathbf{x}_p, \theta_\mathbf{u}, \theta_\mathbf{v})$ and $\chi_\theta^2(\mathbf{x}_c, \mathbf{x}_p)$ functions around the optical center, as illustrated by Figure 4.

2.4 CCD Sensor Array Misalignments

CCD sensor misalignments are due to imperfections at the time of assembly. These imperfections, however minute, introduce additional noise as some types

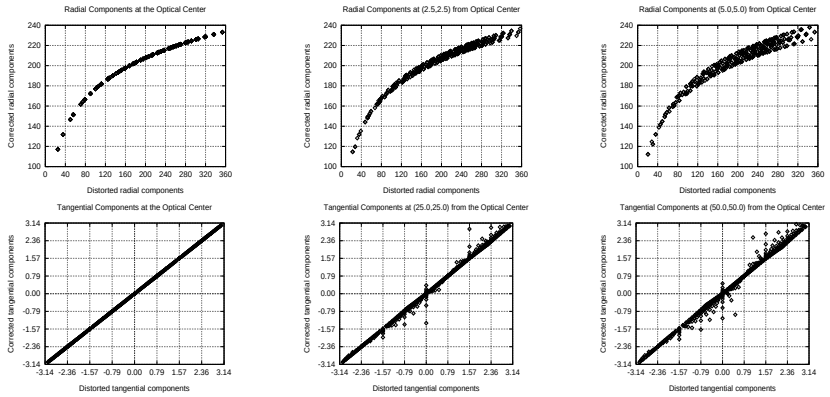

Fig. 3. *Plots of* $(\hat{r}_{ij}, r_{ij})$ *and* $(\hat{\theta}_{ij}, \theta_{ij})$. **a) (top, from left to right):** $\hat{r}_{ij}$ *and* r_{ij} *at the optical center,* $(2.5, 2.5)$ *and* $(5.0, 5.0)$ *image units away from it.* **b) (bottom, from left to right):** $\hat{\theta}_{ij}$ *and* θ_{ij} *at the optical center,* $(25.0, 25.0)$ *and* $(50.0, 50.0)$ *image units away from it. The increasing scattering of the plots as the distance from the optical center increases prevents accurate modelling of the lens. The effect is most apparent for the* r_{ij}*'s, yet it is also observed with the* θ_{ij}*'s.*

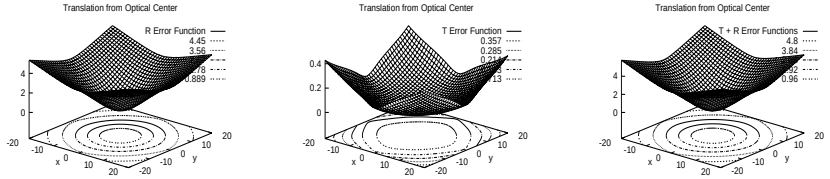

Fig. 4. *Effect of translation from the optical center on* $\chi^2_r(\mathbf{x}_c, \mathbf{x}_p, \theta_\mathbf{u}, \theta_\mathbf{v})$ *and* $\chi^2_\theta(\mathbf{x}_c, \mathbf{x}_p)$. **a) (left):** *Plot of the* $\chi^2_r(\mathbf{x} - \mathbf{x}_c, \mathbf{x}_p, \theta_\mathbf{u}, \theta_\mathbf{v})$ *function.* **b) (center):** *Plot of the* $\chi^2_\theta(\mathbf{x} - \mathbf{x}_c, \mathbf{x}_p)$ *function.* **c) (right):** *Plot of the* $\chi^2_r(\mathbf{x} - \mathbf{x}_c, \mathbf{x}_p, \theta_\mathbf{u}, \theta_\mathbf{v}) + \chi^2_\theta(\mathbf{x} - \mathbf{x}_c, \mathbf{x}_p)$ *function.*

of misalignments influence the value of the $\chi^2_r(\mathbf{x}_c, \mathbf{x}_p, \theta_\mathbf{u}, \theta_\mathbf{v})$ function. We have studied the effect of such misalignments by rotating the image plane of the synthetic camera model about its origin. Figure 5 shows the $\chi^2_r(\mathbf{x}_c, \mathbf{x}_p, \theta_\mathbf{u}, \theta_\mathbf{v})$ and $\chi^2_\theta(\mathbf{x}_c, \mathbf{x}_p)$ functions for rotations $\theta_\mathbf{u}$, $\theta_\mathbf{v}$ and $\theta_\mathbf{n}$ about the $\mathbf{u}$, $\mathbf{v}$ and $\mathbf{n}$ axes of the synthetic camera. The effects have been studied in isolation to one another and, in these experiments, the optical center projected onto the origin of the synthetic camera.

As expected, rotations about the line of sight axis $\mathbf{n}$ have no effect on the $\chi^2_r(\mathbf{x}_c, \mathbf{x}_p, \theta_\mathbf{u}, \theta_\mathbf{v})$ function, as they do not break the point-symmetry of radial distortion. However, rotations about the axes of the image plane $\mathbf{u}$ and $\mathbf{v}$ intro-

duce errors reflected in $\chi_r^2(\mathbf{x}_c, \mathbf{x}_p, \theta_\mathbf{u}, \theta_\mathbf{v})$ (see Figure 5a). As expected, this type of rotation breaks the point-symmetry of radial distortion.

In all three types of rotations, the $\chi_\theta^2(\mathbf{x}_c, \mathbf{x}_p)$ function remains undisturbed, as shown in Figure 5b. Since the position of the optical center is not shifted by the rotations, no violation of the line-symmetry of the tangential distortion is introduced. If such rotations were to be centered away from the image position of the optical center, then errors would be introduced because of the breaking of the line-symmetry. This is also illustrated by Figure 6 where, for the three types of rotation, the plots of $(\hat{\theta}_{ij}, \theta_{ij})$ describe a bijection and do not indroduce approximation errors in the fit, contrary to the plots of $(\hat{r}_{ij}, r_{ij})$ in Figure 3a.

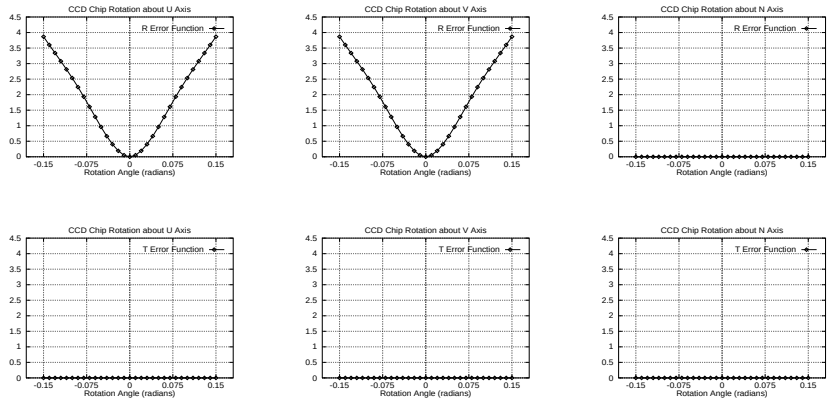

Fig. 5. *Effect of CCD array rotation on* $\chi_r^2(\mathbf{x}_c, \mathbf{x}_p, \theta_\mathbf{u}, \theta_\mathbf{v})$ *and* $\chi_\theta^2(\mathbf{x}_c, \mathbf{x}_p)$ *functions.* **a) (top, from left to right):** *The* $\chi_r^2(\mathbf{x}_c, \mathbf{x}_p, \theta_\mathbf{u}, \theta_\mathbf{v})$ *resudual function against rotations around the* $\mathbf{u}$, $\mathbf{v}$ *and* $\mathbf{n}$ *axes.* **b) (bottom, from left to right):** *The* $\chi_\theta^2(\mathbf{x}_c, \mathbf{x}_p)$ *residual function against rotations around the* $\mathbf{u}$, $\mathbf{v}$ *and* $\mathbf{n}$ *axes.*

Another phenomenon affecting the value of the residual is the alignment of the synthetic pinhole calibration dots with the spherical points as imaged by the lens. Given an ideal situation in which the central calibration point is imaged at the image center and that this location coincides with the optical center, then the residual is at a minimum. However, any deviation from this situation substantially increases the value of the residual, and for certain is by no means related to the calibration parameters of the camera. Additionally, we cannot require that the central calibration dot be imaged at the optical center, since it is one of the parameters to be estimated.

In light of this, we also model translation of the camera parallel to the calibration plane as translation of the synthetic pinhole calibration points $\hat{\mathbf{p}}_{ij}$. Con-

sequently, the calibrtation method must minimize the residual with respect to the following parameters:

- $\mathbf{x}_c$: The amount of translation of imaged spherical points $\mathbf{p}_{ij}$, which models translation of the CCD sensor array in the $(\mathbf{u}, \mathbf{v})$ plane. In other words, $\mathbf{x}_c$ is the translation from the image center to the optical center.
- $\mathbf{x}_p$: The amount of translation of the synthetic pinhole calibration points $\hat{\mathbf{p}}_{ij}$, which models the translation of the camera in the (X,Y) plane, parallel to the calibration surface.
- $\theta_{\mathbf{u}}$, $\theta_{\mathbf{v}}$: The pitch and yaw angles of the CCD sensor array.

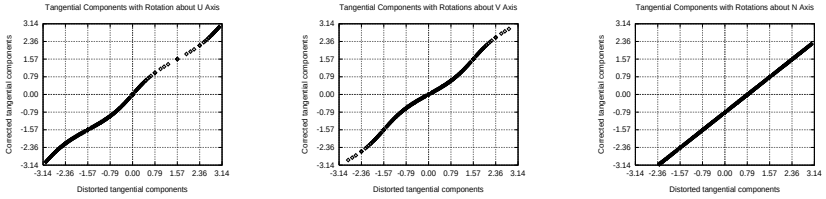

Fig. 6. *Plots of* $(\hat{\theta}_{ij}, \theta_{ij})$ *under rotations of 0.8 radians around* **a) (left):** *the* $\mathbf{u}$ *axis,* **b) (center)** *the* $\mathbf{v}$ *axis and* **c) (right):** *the* $\mathbf{n}$ *axis.*

3 Synthetic Camera Model

We calibrate against a standard, synthetic pinhole camera described by linear transformation matrices containing the instrinsic parameters to be calibrated. The first transformation is from the world coordinate system to that of the synthetic camera, expressed by the camera position $\mathbf{r}$ in world coordinates and orthogonal unit vectors $\mathbf{u} = (u_x, u_y, u_z)^T$, $\mathbf{v} = (v_x, v_y, v_z)^T$ and $\mathbf{n} = (n_x, n_y, n_z)^T$. In addition, since the vector joining the image plane at the optical center and the focal point may not be perpendicular to the image plane, we model the focal length in the coordinate system of the camera as a vector $\mathbf{f} = (f_u, f_v, f_n)^T$. The translation from optical center to image center $\mathbf{x}_c = (x_c, y_c)^T$ and the scaling factors s_x and s_y from synthetic camera image to real image also are parameters forming the synthetic camera model. Combining these into a homogeneous linear transformation yields the matrix C:

$$\begin{pmatrix} s_x u_x - f_n^{-1} n_x (f_u s_x - x_c) & s_y v_x - f_n^{-1} n_x (f_v s_y - y_c) & n_x & -f_n^{-1} n_x \\ s_x u_y - f_n^{-1} n_y (f_u s_x - x_c) & s_y v_y - f_n^{-1} n_y (f_v s_y - y_c) & n_y & -f_n^{-1} n_y \\ s_x u_z - f_n^{-1} n_z (f_u s_x - x_c) & s_y v_z - f_n^{-1} n_z (f_v s_y - y_c) & n_z & -f_n^{-1} n_z \\ s_x r'_x - f_n^{-1} r'_z (f_u s_x - x_c) + x_c & s_y r'_y - f_n^{-1} r'_z (f_v s_y - y_c) + y_c & r'_z & f_n^{-1} r'_z + 1 \end{pmatrix}$$

where $r'_x = -\mathbf{r}^T\mathbf{u}$, $r'_y = -\mathbf{r}^T\mathbf{v}$ and $r'_z = -\mathbf{r}^T\mathbf{n}$. Planar points $\mathbf{P}_{ij}$ are projected onto the imaging plane of the pinhole camera as $C^T\mathbf{P}_{ij} = \hat{\mathbf{p}}_{ij}$. To obtain the points $\mathbf{p}_{ij}$ as imaged by a hypothetical spherical lens, we use the fish-eye transform due to Basu and Licardie to distort the $\hat{\mathbf{p}}_{ij}$'s. The fish-eye transformation is given by

$$\mathbf{p}_{ij} = s\log(1 + \lambda\|\hat{\mathbf{p}}_{ij}\|_2)\boldsymbol{\rho}_{ij} \tag{13}$$

where $\mathbf{p}_{ij} = (x_{ij}, y_{ij})^T$, $\hat{\mathbf{p}}_{ij} = (\hat{x}_{ij}, \hat{y}_{ij})^T$, $\boldsymbol{\rho}_{ij} = (\cos\xi, \sin\xi)^T$, and $\xi = \tan^{-1}\frac{\hat{y}_{ij}}{\hat{x}_{ij}}$. The symbols s and λ are scaling and radial distortion factors, respectively.

4 Description of Algorithm

As a first step, we generate calibration points using the synthetic pinhole camera. The analytic calibration plane is conveniently located in the (X, Y) plane of the world coordinate system and the line of sight of the pinhole camera coincides with the Z axis.

The synthetic image plane is at 340 mm from the calibration plane and the focal length is set to 100 mm. The pinhole calibration points are then projected onto the image plane of the synthetic camera as $C^T\mathbf{P}_{ij} = \hat{\mathbf{p}}_{ij}$ and kept in polar coordinates as $(\hat{r}_{ij}, \hat{\theta}_{ij})$.

Using the spherical camera, oriented perpendicularly from the real calibration plane, a frame of the calibration points is grabbed. The lens of the spherical camera is at 280 mm from the calibration plane. Figure 7b and c show such frames. We perform point detection on this image by computing the centroids of the calibration points and obtain spherical image points (r_{ij}, θ_{ij}). Both sets of points $(\hat{r}_{ij}, \hat{\theta}_{ij})$ and (r_{ij}, θ_{ij}) are scaled to the canonical space $[(-1, -\frac{\pi}{2}), (1, \frac{\pi}{2})]$ where the minimization procedure is to begin.

We use a gonjugate gradient minimization procedure due to Polak-Ribiere [8] which we apply on the function $\chi^2 = \chi^2_r(\mathbf{x}_c, \mathbf{x}_p, \theta_\mathbf{u}, \theta_\mathbf{v}) + \chi^2_\theta(\mathbf{x}_c, \mathbf{x}_p)$. In order to perform the minimization, the partial derivatives $\frac{\partial\chi^2}{\partial x_c}$, $\frac{\partial\chi^2}{\partial y_c}$, $\frac{\partial\chi^2}{\partial x_p}$, $\frac{\partial\chi^2}{\partial y_p}$, $\frac{\partial\chi^2}{\partial\theta_\mathbf{u}}$ and $\frac{\partial\chi^2}{\partial\theta_\mathbf{v}}$ need to be evaluated for various values of $(\mathbf{x}_c, \mathbf{x}_p, \theta_\mathbf{u}, \theta_\mathbf{v})$.

To evaluate the partial derivatives with respect to $\mathbf{x}_c$, we perform translations of the detected spherical calibration points $\mathbf{p}_{ij} = (r_{ij}, \theta_{ij})$ onto the image plane and perform least-squares fits to obtain the χ^2 values then used for computing 5-point central differences. Evalutation of partial derivatives with respect to CCD array angles is more involved. The first step is to reproject the pinhole calibration points $\hat{\mathbf{p}}_{ij}$ back onto the calibration plane using C^{-1}, the inverse of the pinhole camera transformation. Rotations of these reprojected points in 3D and reprojection onto the image plane of the pinhole camera provide the χ^2 values for computing 5-point central differences. The minimzation is performed with the shifted and rotated calibration points and is guided by the 6D gradient vector $(\frac{\partial\chi^2}{\partial x_c}, \frac{\partial\chi^2}{\partial y_c}, \frac{\partial\chi^2}{\partial x_p}, \frac{\partial\chi^2}{\partial y_p}, \frac{\partial\chi^2}{\partial\theta_\mathbf{u}}, \frac{\partial\chi^2}{\partial\theta_\mathbf{v}})$. The output of the algorithm is the optical center $\mathbf{x}_c$, represented as the shift from the image center, the camera translation $\mathbf{x}_p$ parallel to the calibration surface with respect to the central calibration point,

the CCD sensor array pitch and yaw angles $\theta_{\mathbf{u}}$ and $\theta_{\mathbf{v}}$ and the polynomials in r and θ for image transformation from spherical to pinhole. In essence, the procedure is to find the parameter values that best explain the detected calibration points as imaged by the spherical lens.

5 Numerical Results

We study the convergence rate of the calibration procedure, its resistance to input noise and the results obtained with the calibration images of Figure 7b and c, corresponding to spherical cameras A and B, respectively. Figure 7a shows a typical frame taken by a spherical camera, while 7b and c show frames of the calibration plane grabbed with our spherical cameras A and B. The calibration plane has a width and height of 8 feet and the 529 calibration dots are spaced by 4 inches both horizontally and vertically. In order to capture the calibration images, the spherical cameras are mounted on a tripod and approximately aligned with the central calibration dot. The sperical lenses are at a distance of 280 mm from the calibration plane.

The convergence and noise resistance study is performed with a simulated spherical lens. We use equation (13) in order to compute the spherical points $\mathbf{p}_{ij}$ from the synthetic pinhole calibration dots $\hat{\mathbf{p}}_{ij}$. To model CCD sensor array misalignments, we perform 3D rotations of the synthetic pinhole camera and reproject the synthetic calibration points onto the so rotated image plane prior to using (13). In addition, we translate the spherical calibration points $\mathbf{p}_{ij}$ to model the distance of the optical center from the center of the image and also translate the synthetic pinhole calibration points $\hat{\mathbf{p}}_{ij}$ to model the camera translation parallel to the calibration surface.

Input noise is introduced in each synthetic pinhole calibration dot $\mathbf{p}_{ij}$ as Gaussian noise with standard deviations σ_x and σ_y expressed in image units (pixels). This step is performed before using (13) and models only the positional inaccuracy of calibration dots. We proceed to evaluate the performance of the calibration procedure with respect to convergence rates and input noise levels with a simulated spherical lens and present experiments on real spherical camera images (our spherical cameras A and B) for which we have computed their calibration parameters.

5.1 Convergence Analysis

In order to study the convergence rate of the calibration method, we monitored the values of the error function χ^2 with respect to the number of iterations performed in the 6D minimization procedure using the Polak-Ribiere conjugate gradient technique. Figure 8 reports three experiments performed with various calibration parameters. The start of the 6D search always begins at $(\mathbf{x}_c, \mathbf{x}_p, \theta_{\mathbf{u}}, \theta_{\mathbf{v}}) = \mathbf{0}$ and, as expected, the number of required iterations to converge to the solution is proportional to the distance of the calibration parameters to the initial search values. We used a tolerance of 1×10^{-8} on convergence and

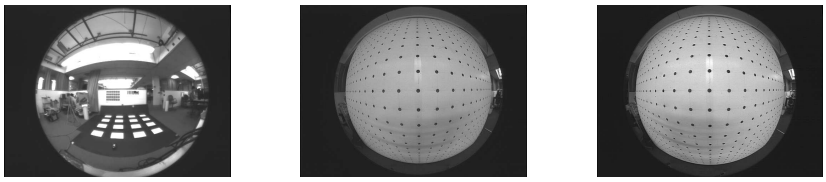

Fig. 7. a) (left): *A typical image from a spherical lens camera.* **b) (center):** *Image of the calibration plane grabbed with spherical camera A.* **c) (right):** *Image of the calibration plane grabbed with spherical camera B.*

we computed the various derivatives of the error function χ^2 with 5-point differences with intervals of 0.2 image units for translation and intervals of 0.0002 radians for rotations.

As figure 8 demonstrates, convergence rates are steep and, in general, 40 iterations are sufficient to obtain adequate calibration parameters. Figure 8a shows the convegence for calibration parameters $(\mathbf{x}_c, \mathbf{x}_p, \theta_\mathbf{u}, \theta_\mathbf{v}) = (5.0, 5.0, -0.1, 0.01)$; Figure 8b) shows the convergence for calibration parameters $(15.0, -5.0, 0.0, 0.2)$ and Figure 8c, for $(15.0, -15.0, -0.1, 0.2)$.

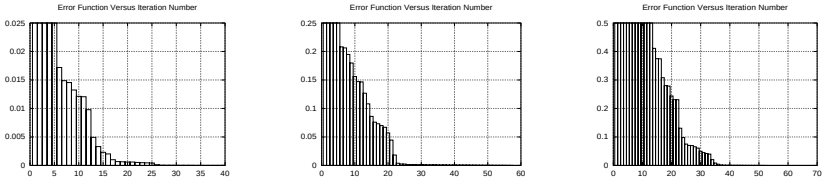

Fig. 8. *Convergence analysis of χ^2 for various configurations of calibration parameters* $(\mathbf{x}_c, \mathbf{x}_p, \theta_\mathbf{u}, \theta_\mathbf{v})$. **a) (left):** $(5.0, 5.0, -0.1, 0.01)$. **b) (center):** $(15.0, -5.0, 0.0, 0.2)$. **c) (right):** $(15.0, -15.0, -0.1, 0.2)$.

5.2 Noise Robustness Analysis

In order to determine the robustness of the procedure with respect to input noise, we introduced various levels of Gaussian noise into the synthetic pinhole calibration dots. We used zero-mean Gaussian noise levels of $\|(\sigma_x, \sigma_y)\|_2 = 0, 1.4142, 2.8284, 4.2426, 5.6569$ and 7.0711, expressed in image units. The effects

of noise onto the calibration parameters $\mathbf{x}_c$, $\mathbf{x}_p$, $\theta_{\mathbf{u}}$ and $\theta_{\mathbf{v}}$ and the the values of the residual χ^2 are depicted by the graphs of Figure 9, which show these values for the noise levels we chose. As can be observed, the ground truth calibration parameters $(\mathbf{x}_c, \mathbf{x}_p, \theta_{\mathbf{u}}, \theta_{\mathbf{v}}) = \mathbf{0}$ show a linear behavior to input noise whereas the residual shows a quadratic growth with respect to input noise.

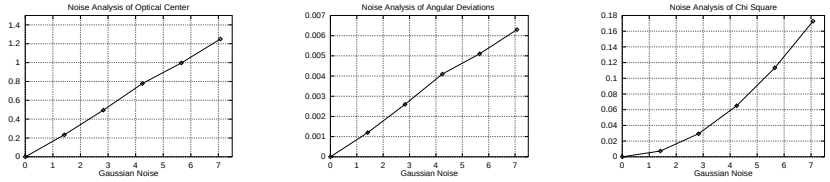

Fig. 9. *The effect of input zero-mean Gaussian noise on the calibration parameters and the residual* χ^2. **a) (left):** *The behavior of* $\|\mathbf{x}_c\|_2$ *with respect to input noise levels* $\|(\sigma_x, \sigma_y)\|_2$. **b) (center):** *The behavior of* $\|(\theta_{\mathbf{u}}, \theta_{\mathbf{v}})\|_2$ *and* **c) (right):** *the behavior of* χ^2.

5.3 Calibration of Spherical Images

We have applied our calibration procedure to both of our spherical cameras and determined their calibration parameters. Tables 1 and 2 show the parameters obtained from spherical cameras A and B, respectively. Figure 10 and 11 show the synthetic pinhole calibration points, the spherical points detected from calibration images 7b and c, and the polynomial reconstruction of those detected points with the calibration coefficients a_i and b_i.

As figure 10c demonstrates, our spherical camera A has a serious assembly misalignment. The yaw angle is in excess of 0.16 radians. However, spherical camera B does not show such misalignments and Figure 11c shows a quasi fronto-parallel polynomial reconstruction of the detected spherical calibration points. In the case of camera A, the misalignment of the CCD array is visible by careful visual examination of the device.

5.4 Removing Distortion in Spherical Images

The transformation polynomials $\hat{\theta}_{ij}$ and $\hat{r}_{ij}$ represent a mapping from spherical to perspective image locations. However, to compensate for distortion, the inverse transformation is required and, in general, the inverse of a polynomial function cannot be found analytically. In light of this, we use the calibration parameters obtained during the modelling phase to:

Calibration Parameters for Spherical Camera A					
Tangential Distortion Coefficients a_i					
a_1	a_2	a_3	a_4	a_5	a_6
-0.0039	3.3274	-0.0216	-0.1836	0.0166	-1.3416
a_7	a_8	a_9	a_{10}	a_{11}	a_{12}
-0.1516	0.6853	0.2253	-0.3347	-0.0879	-0.0092
Radial Distortion Coefficients b_i					
b_1	b_2	b_3	b_4	b_5	b_6
199.6790	-2634.8104	13799.4582	-26999.8134	8895.5168	23348.2599
b_7	b_8	b_9	b_{10}	b_{11}	b_{12}
4858.0468	-17647.3126	-24277.7749	-12166.4282	12108.0938	40070.6891
Singular Values ω_i for χ^2_θ					
ω_1	ω_2	ω_3	ω_4	ω_5	ω_6
23.0001	16.2318	9.6423	5.4287	2.6397	1.3043
ω_7	ω_8	ω_9	ω_{10}	ω_{11}	ω_{12}
0.5012	0.2400	0.0736	0.0325	0.0068	0.0028
Singular Values ω_i for χ^2_r					
ω_1	ω_2	ω_3	ω_4	ω_5	ω_6
525.1062	50.7337	22.1506	7.6035	2.3874	0.6154
ω_7	ω_8	ω_9	ω_{10}	ω_{11}	ω_{12}
0.1383	0.0260	0.0	0.0	0.0	0.0
x_c	y_c	$\theta_{\mathbf{u}}$	$\theta_{\mathbf{v}}$	χ^2	
-0.0753	-3.2792	-0.0314	-0.1722	0.0543	

Table 1. *The calibration parameters for spherical camera A.*

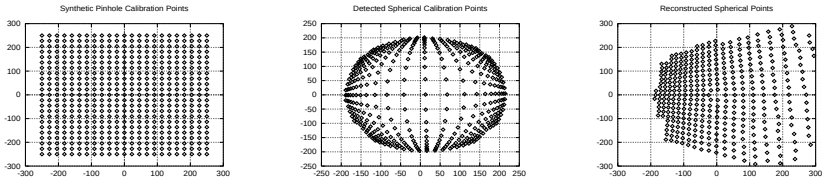

Fig. 10. *Calibration experiment with spherical camera A.* **a) (left):** *The pinhole calibration points, as imaged by the synthetic camera.* **b) (center):** *The spherical points as detected from image in Figure 7b.* **c) (right):** *The polynomial reconstruction obtained for this set of calibration points.*

Calibration Parameters for Spherical Camera B					
Tangential Distortion Coefficients a_i					
a_1	a_2	a_3	a_4	a_5	a_6
-0.0097	3.1918	-0.0053	-0.2562	0.0658	0.1847
a_7	a_8	a_9	a_{10}	a_{11}	a_{12}
-0.1615	0.4940	0.1577	-0.8093	-0.0553	0.3371
Radial Distortion Coefficients b_i					
b_1	b_2	b_3	b_4	b_5	b_6
-30.4219	458.6032	-1240.1970	1394.3862	1003.5856	-610.6167
b_7	b_8	b_9	b_{10}	b_{11}	b_{12}
-1433.4416	-1063.6945	54.0374	1359.5348	2472.7284	3225.6347
Singular Values ω_i for χ^2_θ					
ω_1	ω_2	ω_3	ω_4	ω_5	ω_6
23.6078	17.0001	9.9003	5.6505	2.7189	1.3567
ω_7	ω_8	ω_9	ω_{10}	ω_{11}	ω_{12}
0.5264	0.2489	0.0770	0.0336	0.0071	0.0030
Singular Values ω_i for χ^2_r					
ω_1	ω_2	ω_3	ω_4	ω_5	ω_6
29.7794	10.8641	3.6978	1.0619	0.2580	0.0536
ω_7	ω_8	ω_9	ω_{10}	ω_{11}	ω_{12}
0.0095	0.0014	0.0	0.0	0.0	0.0
x_c	y_c	$\theta_{\mathbf{u}}$	$\theta_{\mathbf{v}}$	χ^2	
0.0118	-0.8273	0.0091	0.0031	0.1188	

Table 2. *The calibration parameters for spherical camera B.*

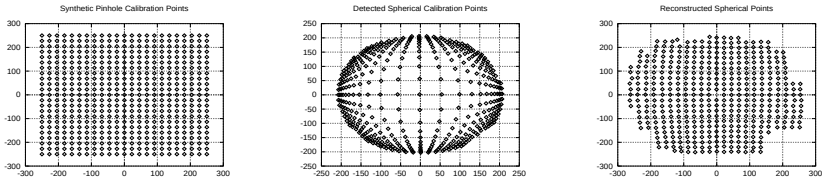

Fig. 11. *Calibration experiment with spherical camera B.* **a) (left):** *The pinhole calibration points, as imaged by the synthetic camera.* **b) (center):** *The spherical points as detected from image in Figure 7c.* **c) (right):** *The polynomial reconstruction obtained for this set of calibration points.*

1. shift and rotate the planar image points to construct by $\mathbf{x}_p$, $\theta_{\mathbf{u}}$ and $\theta_{\mathbf{v}}$ respectively;
2. shift the detected spherical points by $-\mathbf{x}_c$;

and compute the polynomial coefficients of the inverse transformation as

$$\theta_{ij} = \sum_{k=0}^{L} a_k \hat{\theta'}_{ij} \quad \text{and} \quad r_{ij} = \sum_{k=0}^{L} b_k \hat{r}'_{ij} \tag{14}$$

using a procedure identical to solving (4). The polynomials in (14) are the pseudo-inverses of (4) and are used to remove radial and tangential distortions from spherical images. Figures 12 and 13 show the distortion removal on the calibration images and on a typical stereo pair acquired with the spherical cameras. A lookup table without interpolation (linear or other) was used to implement the transformation.

5.5 Image Processing Issues

Removing distortions from spherical images is not as important as the transformation of image processing results into a perspective space. The advantages of such approaches are many. For instance, the costly transformation of complete image sequences is avoided; image processing algorithms directly applied to spherical images do not suffer from the noise introduced with the distortion removal process, and the results of image processing algorithms are generally more compact with respect to the original signal and hence faster to transform to a perspective space.

6 Conclusion

Spherical cameras are variable-resolution imaging systems that have been recognized as promising devices for autonomous navigation purposes, mainly because of their wide viewing angle which increases the capabilities of vision-based obstacle avoidance schemes. In addition, spherical lenses resemble the primate eye in their projective models and are biologically relevant. We presented a novel method for spherical-lens camera calibration which models the lens radial and tangential distortions and determines the optical center and the angular deviations of the CCD sensor array within a unified numerical procedure. Contrary to other methods, there is no need for special equipment such as low-power laser beams or non-standard numerical procedures for finding the optical center. Numerical experiments and robustness analyses are presented and the results have shown adequate convergence rates and resistance to input noise. The method was successfully applied to our pair of spherical cameras and allowed us to diagnose a severe CCD array misalignment of camera A.

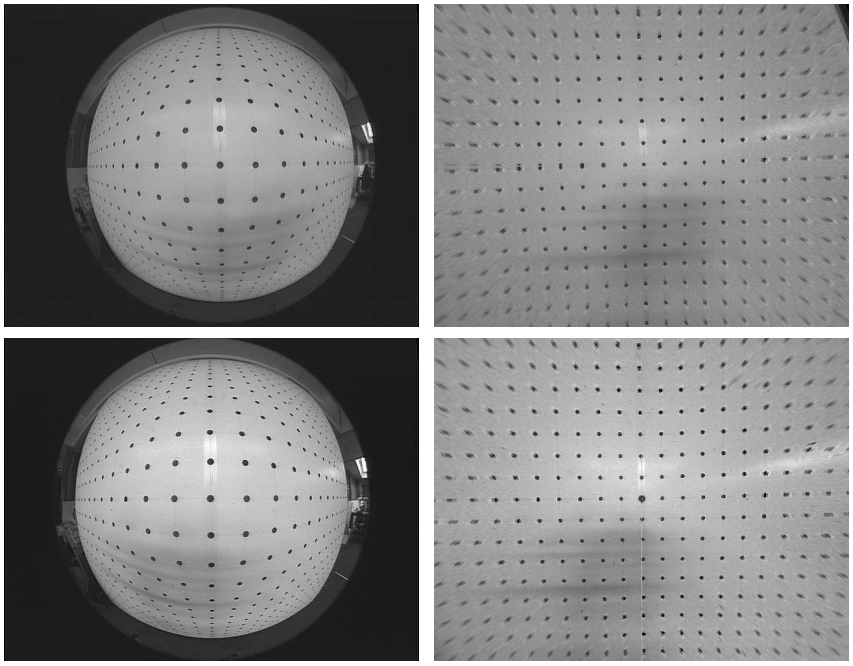

Fig. 12. *Disrtortion removal from calibration images.* **(left):** *Camera A.* **(right):** *Camera B.*

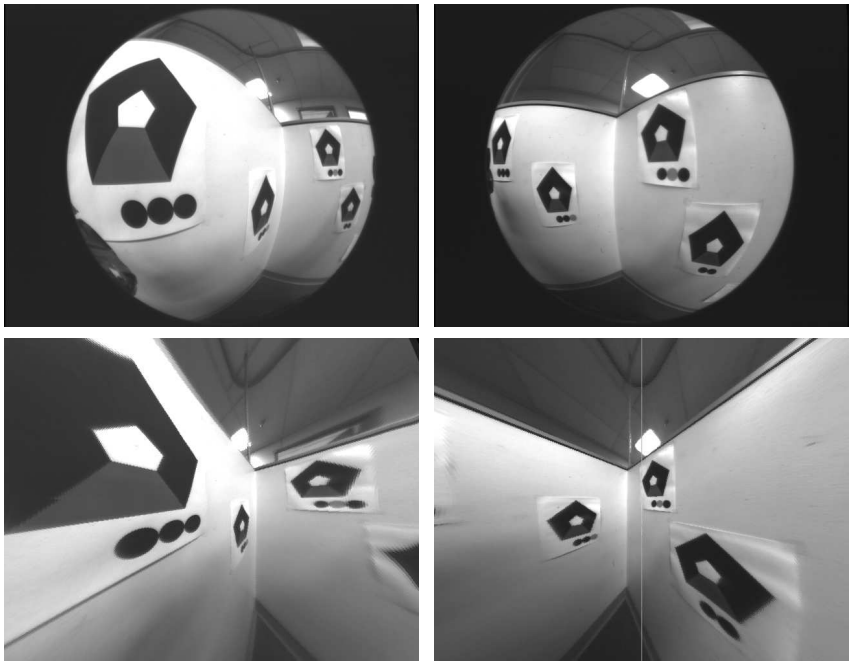

Fig. 13. *Disrtortion removal from typical images.* **(left):** *Camera A.* **(right):** *Camera B.*

A Point Detection Algorithm

We use a calibration plane with a grid of $n \times n$ points (where n is odd) for the calibration process. Using a spherical camera perpendicular to the calibration plane, frames of the calibration points are acquired. In this section we describe the algorithm used to detect the calibration points on this spherical image.

The grid points are numbered according to their position in the image plane coordinate system. The central point is $\mathbf{p}_{00}$, the points on the x-axis are defined from left to right by $\{\mathbf{p}_{i0}\}$ where $-m \leq i \leq m$, $m = \frac{n-1}{2}$ and the points of the y-axis from bottom to top by $\{\mathbf{p}_{0j}\}$, $-m \leq j \leq m$. $\mathbf{p}_{ij}$ is the point that lies in the j^{th} row and the i^{th} column of the grid, relative to the origin. The value of $\mathbf{p}_{ij}$ is a 2D vector of its centroid position or **fail** for a point that was not detected.

An iterative algorithm is used to detect the grid points. In the first iteration ($k = 0$) the point at the center of the grid, $\mathbf{p}_{00}$, is detected. In the k^{th} iteration, $1 \leq k \leq 2m$, all the points $\mathbf{p}_{ij}$ such that $|i| + |j| = k$ are found. The first step in detecting any grid point is defining an image pixel from which the search for this point is to begin. The initial pixel is used as an input to the **detect** procedure which outputs the centroid of the requested grid point, or **fail** if the point is not found.

The initial pixel for searching the central point is the pixel at the center of the image. For any other point, the positions of neighboring grid points that were detected in earlier iterations are used to define the initial pixel. When detecting a grid point $\mathbf{p}_{i0}$ on the x-axis, the initial pixel depends on the location of $\mathbf{p}_{i'0}$ which is the point next to $\mathbf{p}_{i0}$ and closer to the center. The initial pixel in this case is calculated by adding to $\mathbf{p}_{i'0}$ a vector $\mathbf{c}_{i'}$ with magnitude equal to the width of the grid point $\mathbf{p}_{i'0}$ directed from the center towards $\mathbf{p}_{i'0}$. The initial pixel used for detecting points on the y-axis is calculated in a similar way. When detecting the point $\mathbf{p}_{ij}$ in iteration k, the points $\mathbf{p}_{i'j'}$, $\mathbf{p}_{ij'}$ and $\mathbf{p}_{i'j}$ are already detected in iterations $k-1$ and $k-2$. We start the search for $\mathbf{p}_{ij}$ from the pixel defined by $\mathbf{p}_{ij'} + \mathbf{p}_{i'j} - \mathbf{p}_{i'j'}$ (see figure 14).

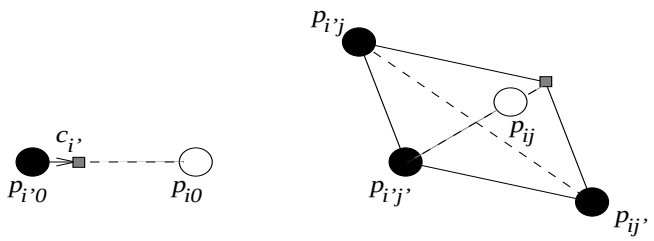

Fig. 14. a) (left): *Finding point* $\mathbf{p}_{i0}$ *based on* $\mathbf{p}_{i'0}$. **b) (right):** *Finding point* $\mathbf{p}_{ij}$ *based on* $\mathbf{P}_{i'j'}$, $\mathbf{p}_{ij'}$ *and* $\mathbf{p}_{i'j}$. *The gray rectangle marks the initial pixel.*

```
p_00 ← detect(0, 0)
for k = 1 to 2m
    for each p_ij such that |i| + |j| = k do
        i' = sign(i) · (|i| − 1)
        j' = sign(j) · (|j| − 1)
        if i = 0 then
            if p_i'0 ≠ fail then
                p_i0 ← detect(p_i'0 + c_i')
            else p_i0 ← fail
        else if j = 0 then
            if p_0j' ≠ fail then
                p_0j ← detect(p_0j' + c_j')
            else p_0j ← fail
        else if p_ij', p_i'j, p_i'j' ≠ fail then
            p_ij ← detect(p_ij' + p_i'j − p_i'j')
        else p_ij ← fail
```

Fig. 15. *Algorithm for detecting grid points on a spherical image.*

The **detect** procedure uses a threshold mechanism to separate the pixels that are within the grid points from the background pixels. Since the image contains areas with different illumination levels, we use multi-level thresholding to detect the points in all areas of the image.

We define an initial threshold level as the minimum gray level such that at least 4% of the image pixels are below the threshold. The **detect** procedure finds a pixel closest to the input pixel with a gray level that is lower than the defined threshold. It assumes that this pixel is contained within the grid point. If no such pixel is found, the threshold is increased and the search is repeated until such pixel is found or until the threshold gets the maximum gray value (white). In the later case the procedure returns **fail**. If a pixel with a low gray level is found, all the neighboring pixels with gray levels that are lower than the threshold are grouped to form a grid point. The smallest rectangle that bounds the grid point is found. The center of the grid point is the mean of the pixels contained in the bounding rectangle calculated in the following way: let R be the bounding rectangle, where $R = \{(x, y) | x_1 \leq x \leq x_2 \text{ and } y_1 \leq y \leq y_2\}$, then the mean over the pixels in R is:

$$M_x(R) = \frac{\sum_{x=x_1}^{x_2} \sum_{y=y_1}^{y_2} x(C - \mathbf{I}(x,y))}{\sum_{x=x_1}^{x_2} \sum_{y=y_1}^{y_2} C - \mathbf{I}(x,y)} \quad M_y(R) = \frac{\sum_{x=x_1}^{x_2} \sum_{y=y_1}^{y_2} y(C - \mathbf{I}(x,y))}{\sum_{x=x_1}^{x_2} \sum_{y=y_1}^{y_2} C - \mathbf{I}(x,y)} \tag{15}$$

where $\mathbf{I}(x, y)$ is the gray level of the pixel (x, y) and C is the maximum grayvalue. If the bounding rectangle contains more than just the grid point, which might be the case with a high threshold the procedure returns **fail**.

References

1. R. L. Anderson, N. Alvertos, and E. L. Hall. Omnidirectional real time imaging using digital restoration. *SPIE High Speed Photograph*, 348, 1982.
2. S. Baker and S. K. Nayar. A theory of catadioptric image formation. In *Proceedings of ICCV*, pages 35–42, Bombay, India, January 1998.
3. A. Basu and S. Licardie. Alternative models for fish-eye lenses. *Pattern Recognition Letters*, 16(4):433–441, 1995.
4. Y. Kuniyoshi, N. Kita, and K. Sugimoto. A foveated wide angle lens for active vision. In *IEEE Proceedings Robotics and Automation*, 1995.
5. K. Myiamoto. Fish eye lens. *J. Lett.*, pages 1060–1061, 1964.
6. Y. Nomura, M. Sagara, H. Naruse, and A. Ide. Simple calibration algorithm for high-distortion-lens camera. *IEEE PAMI*, 14(11):1095–1099, 1992.
7. American Society of Photogrammetry. *Manual of Photogrammetry, 4th edition.* 1980.
8. E. Polak. *Computational Methods in Optimization.* Academic Press, New-York, 1971.
9. S. Shah and J. K. Aggarwal. Autonomous mobile robot navigation using fish-eye lenses. *Image Analysis Applications and Computer Graphics*, 1024:9–16, 1995.
10. S. Shah and J. K. Aggarwal. Intrinsic parameter calibration procedure for a (high distortion) fish-eye lens camera with distortion model and accuracy estimation. *Pattern Recognition*, 29(11):1775–1778, 1996.
11. S. Shah and J. K. Aggarwal. Mobile robot navigation and scene modeling using stereo fish-eye lens system. *Machine Vision and Applications*, 10(4):159–173, 1997.
12. S. W. Shih, Y. P. Hung, and W. S. Lin. When should we consider lens distortion in camera calibration. *Pattern Recognition*, 28(3):447–461, 1995.
13. R. Y. Tsai. A versatile camera calibration technique for high-accuracy 3d machine vision metrology using off-the-shelf tv cameras and lenses. *IEEE Journal of Robotics and Automation*, 3(4):323–344, 1987.
14. J. Weng, P. Cohen, and M. Herniou. Camera calibration with distortion models and accuracy evaluation. *IEEE PAMI*, 14(10):965–980, 1992.